Energy Flow Path Planning and Multiload Constant Voltage Outputs in Domino WPT System Based on Current Phase Configuration

Yanling Li, *Member, IEEE*, Yongkang Jiang, Weiqiang Liu, Jingxian Zhao, Yong Li, *Senior Member, IEEE*,
and Zhengyou He, *Senior Member, IEEE*

***Abstract*—Cross-coupling among the domino coils complicates the energy flow paths and prevents the multiload constant outputs in wireless power transfer (WPT) system. To overcome this problem, the current phase of the domino coils is first analyzed so that the impedance relationship of cross-coupling in its corresponding coil loop is found. The analytical formula for computing the resonant compensation capacitance is then derived according to the current phase configuration with 90 degrees of decline gradient. It can achieve the load-independent zero phase angle and constant outputs simultaneously in a single-energy flow transmission mode. Then the domino coils are further extended to the transmission mode with multienergy flow paths that can be planned by configuring the current phase. Finally, a general capacitance calculation method is proposed for different energy flow path planning. Prototypes of seven-coil domino system and six-coil domino system are constructed. Experimental results show that seven-coil domino system with the single energy flow path achieves the constant voltage of 29.55 V and a dc–dc efficiency of 83.69%. Six-coil WPT system also has the constant outputs of 21.34 V and 32.31 V by planning the dual energy flow paths, with a dc–dc efficiency of 79.68%.**

***Index Terms*—Constant voltage output, load-independent, multiple loads, wireless power transfer.**

Received 10 July 2024; revised 7 October 2024 and 1 December 2024; accepted 31 December 2024. Date of publication 7 January 2025; date of current version 26 February 2025. This work was supported in part by the National Natural Science Foundation of China under Grant 62471409, in part by Hebei Natural Science Foundation under Grant E2024105010, in part by Sichuan Science and Technology Program under Grant 2024NSFSC0524, in part by the Fundamental Research Funds for the Central Universities under Grant 2682024ZTPY019, in part by the Fundamental Research Funds for the Central Universities under Grant 2682023ZTPY026, and in part by Chengdu Guojia Electrical Engineering Company Ltd. under Grant NEEC-2022-B06. Recommended for publication by Associate Editor C. Tse. *(Corresponding author: Yanling Li.)*

Yongkang Jiang, Weiqiang Liu, Jingxian Zhao, Yong Li, and Zhengyou He are with the School of Electrical Engineering, Southwest Jiaotong University, Chengdu 611756, China (e-mail: jiangyongkang@my.swjtu.edu.cn; liuweiqiang@my.swjtu.edu.cn; jingxianzhao@my.swjtu.edu.cn; yong_li@swjtu.edu.cn; hezy@home.swjtu.edu.cn).

Yanling Li is with the School of Electrical Engineering, Southwest Jiaotong University, Chengdu 611756, China, and also with the Graduate School of Tangshan, Southwest Jiaotong University, Tangshan 063000, China (e-mail: yanling_li@swjtu.edu.cn).

Color versions of one or more figures in this article are available at https://doi.org/10.1109/TPEL.2025.3526796.

Digital Object Identifier 10.1109/TPEL.2025.3526796

I. INTRODUCTION

DOMINO wireless power transfer (WPT), based on several relay coils between the transmitter and receiver, is a novel way to realize a medium- or long-distance power transmission [1]. Generally, every relay coil should be compensated by a capacitor to form the dielectric resonator, which can improve the power transmission efficiency [2], [3], [4], [5] and output characteristics. Compared to the traditional cable-based power supply system, the domino WPT system offers some benefits such as low maintenance cost, high reliability, and safety. It can provide new power supply solutions for numerous applications, especially in some environments where the high-voltage condition has strict requirements for electrical insulation, or the power needs to be transmitted over a long distance. In recent years, the domino WPT technology has been applied to supply power for industrial equipment, such as the isolated gate drive system of converters [6], [7], [8], the online monitoring system in high-voltage grid and substations [9], [10], [11], the devices over long distances in smart buildings [12], and the balancing system of battery packs [13], etc.

However, due to the complex cross-coupling among domino coils, the resonant matching for every coil loop becomes challenging: there is a lack of quantitative evaluation of the reflection impedance of all cross-coupling in an independent coil loop. At present, the capacitor often calculated by ignoring the cross-coupling cannot be well resonant with the coil. As a result, this problem has prevented it from meeting the load requirement for a stable voltage supply in the domino WPT system.

In order to suppress the influence of cross-coupling on the system, a number of research has been carried out in the academic community. In [14] and [15], an n-coil domino WPT system was first simplified into a two-coil WPT system, and then the zero phase angle (ZPA) input and constant current (CC)/constant voltage (CV) output were respectively realized by selecting the operating frequency. Moreover, similar critical frequencies were obtained in [16] by modeling a quadratic eigenvalue model. In addition to considering the frequency factor, several related researches on compensation topology were proposed to achieve the CC/CV output. For example, a distributed series compensation method was adopted in [17] for the double-layer domino cylindrical solenoid coupler (CSC) in the post insulator to reduce the resistance caused by the stray capacitance. And

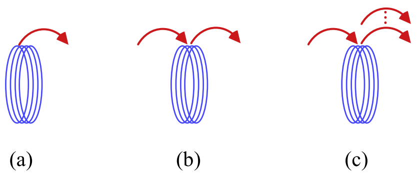

Fig. 1. Energy flow node graph. (a) Transmitting node. (b) Relay node. (c) Energy flow bifurcation node. (d) Receiving node.

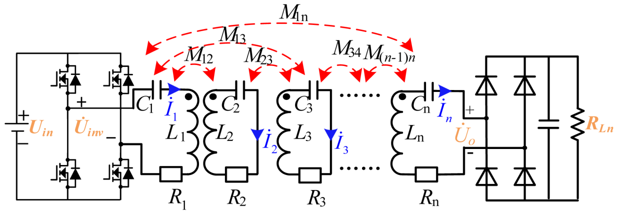

Fig. 2. Schematic diagram of the domino WPT system.

a double-sided LCC-LCC compensated domino WPT system was introduced in [18], where CC/CV output was obtained by adjusting the operating frequency. In addition, an adaptive output adjustment strategy was constructed in [19], where a hybrid topology for the transmitter was used to achieve the CC/CV output. Also, a hybrid compensation network was designed in [20] for the receiving coil, to realize the CC and CV outputs at a fixed frequency by switching between the LCC compensation and the series compensation.

The abovementioned studies have improved the output characteristics for the single-load in the domino WPT system. Nevertheless, they are not suitable for the multiload power supply scenarios that widely exist in the industrial field. Currently, there are three technical ways mainly used for powering the multiple loads in the WPT system, where the coil structure with one transmitter and one receiver [21] needs to be equipped with a multiport dc/dc converter for distributing the power, and the coil structure with n transmitters and n receivers [6] can significantly reduce the isolation voltage between the coils, and another coil structure with one transmitter and n receivers can simplify the structure of the transmitting coil and the compensation circuit [22], [23], [24]. But the cross-coupling among the receiving coils could not be eliminated, leading to the prominent interference among different load branches. In addition, in these studies, the spatial distances between the load and transmitting coil are generally uniform. When the multiple loads that located at different positions are charged, it is very challenging to achieve constant output and meanwhile maintain high transmission efficiency.

To address this challenge, researchers have integrated loads directly into the dielectric resonators [11], [25], [26], [27], [28], [29], [30]. This approach enabled the domino WPT system to have multiple output ports and achieve multiload CC [25], [26] or CV outputs [11], [27], [28], respectively. Mixed multiload CC and CV outputs were implemented in [29] and [30]. However, the existing ones for realizing multiload constant outputs mainly rely on the specialized coil designs and shielding materials to eliminate the coils cross-coupling, which are associated with high costs and limited flexibility in coil designs.

Therefore, this article proposes a novel approach to achieve the CV outputs for multiple loads from the perspective of energy flow paths planning. Energy flow paths include the single energy flow (SEF) path and the multiple energy flow (MEF) paths, whose nodes are classified into four types, as shown in Fig. 1. Fig. 1(a) represents a transmitting node, which is the starting of energy transmission. In Fig. 1(b), a relay node receives the energy from the previous node and transmits it to the next node. The energy flow bifurcation node shown in Fig. 1(c) represents that there are MEF paths injected into the subsequent nodes. And the receiving node in Fig. 1(d) acts as the energy consumption. In addition to the transmitting node and the receiving node, a domino system that also includes the relay node will only have the SEF path, while a system with the energy flow bifurcation node can construct the MEF paths.

For the domino WPT system, the proposed energy flow path planning in the presence of cross-coupling requires the proper current phase configuration for multiload constant outputs. In consequence, the main contributions of this article are as follows.

1) It provides a simple and practical decoupling method for domino coils that only relies on the proper current phase configuration, exemption from the construction of complicated coils' physical structure.
2) For the traditional SEF path transmission mode, an analytical formula for the compensation capacitance is deduced to achieve ZPA and CV/CC output characteristics simultaneously.
3) The general compensation capacitance calculation method for the MEF path transmission mode is given. By planning the MEF paths of the domino WPT system, the multiload CV outputs are achieved.
4) The output characteristics of the system with different energy flow paths are analyzed, and it is concluded that constructing an energy flow bifurcation node on the CC stage coil is necessary for achieving the multiload CV outputs.

The rest of this article is organized as follows. Section II presents the analytical formula of the compensation capacitance for the decoupling of nonadjacent coils in an SEF path system. Based on the current phase configuration, Section III further provides a compensation capacitance calculation method suitable for MEF paths and analyzes the condition for achieving the multiload CV outputs. In Section IV, prototypes of the seven-coil domino system and the six-coil domino system are constructed to validate the proposed energy flow path planning method. Finally, Section V concludes this article.

II. SEF PATH SYSTEM

A. System Structure and Circuit Analysis

A typical domino WPT system circuit, as shown in Fig. 2, includes a transmitting loop, (n-2) relay loops, and a receiving loop. The transmitting loop consists of a dc power source U_{in}, a high-frequency inverter, a transmitting coil, and a series-connected compensation capacitor. A relay coil and its

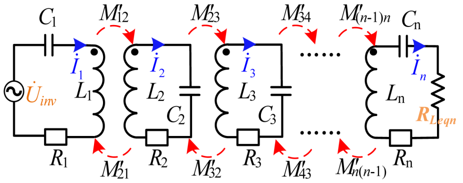

Fig. 3. Schematic diagram after eliminating the cross-coupling.

series-connected compensation capacitor form a relay loop. The receiving loop is comprised of a receiving coil, a series-connected compensation capacitor, a full-bridge rectifier, a filter capacitor, and a load R_{Ln}. In the figure, the transmitting coil, multiple relay coils, and the receiving coil constitute an n-stage energy transfer channel. M_{kj} refers to the mutual inductance between the kth coil and the jth coil ($j \neq k$). The self-inductance of the kth coil is expressed as L_k, and R_k, C_k, I_k are the internal resistance, the series compensation capacitance, and the current of the kth coil respectively, where $k = 1, 2, 3, \ldots, n$.

The equivalent load on the ac side of the full-bridge rectifier can be represented as

$$R_{L\mathrm{eqn}} = \frac{8}{\pi^2} R_{Ln} \tag{1}$$

According to Kirchhoff's voltage and current laws, a mathematical model with the full-impedance relationship of the domino WPT system can be expressed by

$$\begin{bmatrix} U_{\mathrm{inv}} \\ 0 \\ 0 \\ \vdots \\ 0 \end{bmatrix} = \begin{bmatrix} X_{11} & X_{12} & X_{13} & \cdots & X_{1n} \\ X_{21} & X_{22} & X_{23} & \cdots & X_{2n} \\ X_{31} & X_{32} & X_{33} & \cdots & X_{3n} \\ \vdots & \vdots & \vdots & \vdots & \vdots \\ X_{n1} & X_{n2} & X_{n3} & \cdots & X_{nn} + R_{L\mathrm{eqn}} \end{bmatrix} \cdot \begin{bmatrix} \dot{I}_1 \\ \dot{I}_2 \\ \dot{I}_3 \\ \vdots \\ \dot{I}_n \end{bmatrix}. \tag{2}$$

In (2), X_{kk} and X_{kj} are defined as the self-impedance and mutual-impedance of the coils, respectively, with the forms of

$$\begin{aligned} X_{kk} &= R_k + j\left(\omega L_k - 1/\omega C_k\right) \\ X_{kj} &= j\omega M_{kj} \end{aligned} \tag{3}$$

where ω represents the system's resonant angular frequency. According to the existing resonance matching method, ω and the circuit parameters satisfy the relationship in the following equation [31]:

$$\omega = 1 \Big/ \sqrt{L_k C_k} (k = 1, 2 \ldots, n). \tag{4}$$

For domino coils, the interaction between the nonadjacent coils manifests as the cross-coupling, where the reactive power exchange occurs between them, affecting the system's output characteristics. In this article, the idea of back-stepping is adopted. First, from a reverse perspective, it is assumed that the influence of cross-coupling is fully eliminated through the compensation capacitor adjustment, as shown in Fig. 3. Then, the phase relationship of the current between the coils is deduced in reverse and regarded as a condition to eliminate the cross-coupling.

Here, after eliminating the cross-coupling, the remaining mutual inductance $M'_{(k\text{-}1)k}$ and $M'_{k(k\text{-}1)}$ between the adjacent coils, also known as the suppositional mutual inductance, is less than or equal to the measured adjacent mutual inductance. Unlike the traditional definition, it is important to note the suppositional mutual inductance $M'_{(k\text{-}1)k}$ and $M'_{k(k\text{-}1)}$ have different values due to the elimination of distinct first kind of cross-coupling terms, which will be explained further in Section II-C.

Considering that the internal resistance of each coil is generally small in the total impedance of the loop, it can be ignored to simplify the analysis, namely

$$R_1 = R_2 = \cdots R_n = 0. \tag{5}$$

Therefore, the mathematical model of the domino WPT system can be simplified as

$$\begin{bmatrix} U_{\mathrm{inv}} \\ 0 \\ 0 \\ \vdots \\ 0 \end{bmatrix} = \begin{bmatrix} 0 & X'_{12} & 0 & \cdots & 0 \\ X'_{21} & 0 & X'_{23} & \cdots & 0 \\ 0 & X'_{32} & 0 & \cdots & 0 \\ \vdots & \vdots & \vdots & \vdots & \vdots \\ 0 & 0 & 0 & \cdots & R_{L\mathrm{eqn}} \end{bmatrix} \cdot \begin{bmatrix} \dot{I}_1 \\ \dot{I}_2 \\ \dot{I}_3 \\ \vdots \\ \dot{I}_n \end{bmatrix} \tag{6}$$

where X'_{kj} is denoted by

$$X'_{kj} = j\omega M'_{kj}. \tag{7}$$

According to the idea of inversion, (6) describes the phase relationships among coil currents after cross-coupling is eliminated. The general solution of the equation depends on the total number of domino coils. As a result, the expression of the coil currents when n is even is different from that when n is odd.

B. Phase Relationship of Coil Currents

Based on the recursive method, the phase relationship among the coil currents is determined by combining (6) and (7). The current expression for each coil is provided in the following equation:

$$\begin{cases} \dot{I}_1 = \frac{R_{\mathrm{eq2}} \dot{U}_{\mathrm{inv}}}{\omega^2 M'_{12} M'_{21}} \\ \dot{I}_2 = \frac{-j\omega M'_{21} \dot{I}_1}{R_{\mathrm{eq2}}} = \frac{-j\dot{U}_{\mathrm{inv}}}{\omega M'_{12}} \\ \dot{I}_3 = \frac{-j\omega M'_{32} \dot{I}_2}{R_{\mathrm{eq3}}} \\ \qquad \vdots \\ \dot{I}_n = \frac{-j\omega M'_{n(n-1)} \dot{I}_{n-1}}{R_{L\mathrm{eqn}}} \end{cases} \tag{8}$$

where the equivalent impedance of each coil loop conforms to the following equation:

$$\begin{cases} R_{\mathrm{eqn}} = R_{L\mathrm{eqn}} \\ R_{\mathrm{eq}(n-1)} = \frac{\omega^2 M'_{(n-1)n} M'_{n(n-1)}}{R_{\mathrm{eqn}}} \\ \quad \vdots \\ R_{\mathrm{eq2}} = \frac{\omega^2 M'_{23} M'_{32}}{R_{\mathrm{eq3}}} \end{cases}. \tag{9}$$

R_{eqk}($k = 2, 3, \ldots, n\text{-}1$) denotes the impedance of the (k+1)th coil loop reflected to the kth coil loop and R_{eqn} denotes the self-impedance of the nth coil loop.

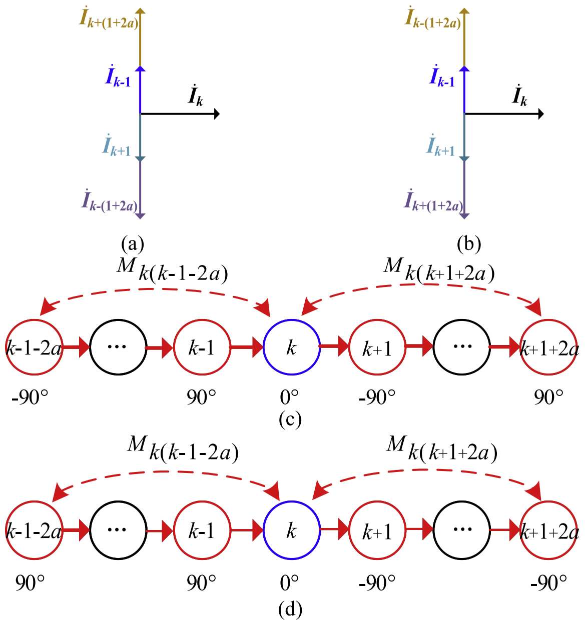

Fig. 4. Current phase of first type of cross-coupling. (a) *a* is odd. (b) *a* is even. (c) Coil node graph when *a* is odd. (d) Coil node graph when *a* is even.

From (8), it is evident that for the *n*-stage domino coils, the current phase difference between adjacent coils exhibits a sequential lag of 90°. Furthermore, when *n* is odd, the current phase of the *n*th coil is either $-180°$ (out of phase) or 0° (in phase) with the input voltage phase, and the *n*th coil will function as a CV stage coil and maintain a CV U_{n_odd} independent of the load, as shown in (10). When *n* is even, the current phase of the *n*th coil is either 90° or -90° with the input voltage phase, and the *n*th coil will function as a CC stage coil and maintain a CC I_{n_even} independent of the load, as shown in (11)

$$U_{n\_\text{odd}} = U_{\text{inv}} \frac{\prod_{k=(n-1)/2,\ldots,2,1} M'_{(2k+1)(2k)}}{\prod_{k=(n-1)/2,\ldots,2,1} M'_{(2k-1)(2k)}} \tag{10}$$

$$I_{n\_\text{even}} = \frac{U_{\text{inv}}}{\omega} \frac{\prod_{k=n/2-1,\ldots,2,1} M'_{(2k+1)(2k)}}{\prod_{k=n/2,n/2-1,\ldots,2,1} M'_{(2k-1)(2k)}}. \tag{11}$$

According to the current expression of each coil, the system transmission efficiency η is derived as

$$\eta = \frac{I_n^2 R_{\text{Leqn}}}{U_{\text{inv}} I_1}. \tag{12}$$

C. *Cross-Coupling Analysis and Analytical Formula of Compensation Capacitor*

Taking the *k*th coil as an example, the cross-coupling between the *k*th coil and the other coils can be classified based on the current phase relationship between the coils.

The first type is the cross-coupling $M_{k(k\pm(1+2a))}$ between the $(k\pm(1+2a))$th coil and the *k*th coil, where $1 \leq k\pm(1+2a) \leq n$ and *a* is a positive integer. The current phase of $(k\pm(1+2a))$th coil advances or lags the current phase of *k*th coil by 90°, as shown in Fig. 4.

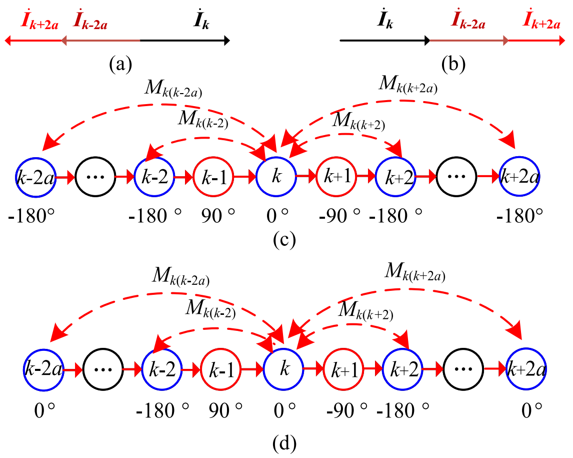

Fig. 5. Current phase of second type of cross-coupling. (a) *a* is odd. (b) *a* is even. (c) Coil node graph when *a* is odd. (d) Coil node graph when *a* is even.

Considering the inherent 90° phase relationship, the first type of cross-coupling can be automatically eliminated by the adjacent mutual inductance $M_{k(k\pm1)}$ between the *k*th coil and the $(k\pm1)$th coil. Therefore, the adjacent mutual inductance $M_{k(k\pm1)}$ measured in practice can be transformed into the suppositional or equivalent adjacent mutual inductance $M'_{k(k\pm1)}$, according to the relationship shown in the following equation:

$$\begin{cases} \dot{I}_{k+1} j\omega M'_{k(k+1)} = G(k), k = 1 \\ \sum_{i=k\pm1} \dot{I}_i j\omega M'_{ki} = J(k) + G(k), 1 < k < n \\ \dot{I}_{k-1} j\omega M'_{k(k-1)} = J(k), k = n \end{cases} \tag{13}$$

where the expressions for *G*(*k*) and *J*(*k*) are

$$G(k) = \sum_{a=0}^{\frac{n-1-k}{2}} \dot{I}_{k+(1+2a)} \cdot j \cdot \omega \cdot M_{k(k+(1+2a))}$$

$$J(k) = \sum_{a=0}^{\frac{k-2}{2}} \dot{I}_{k-(1+2a)} \cdot j \cdot \omega \cdot M_{k(k-(1+2a))}.$$

The right-side of (13) represents the sum of the induced voltages generated by the adjacent mutual inductance $M_{k(k\pm1)}$ and the first type of cross-coupling $M_{k(k\pm(1+2a))}$ in the *k*th coil. And the left-side of (13) denotes the sum of the induced voltages generated by the suppositional adjacent mutual inductance $M'_{k(k\pm1)}$ in the *k*th coil. From (13), it can be seen that the suppositional adjacent mutual inductance is related to the current and the practical mutual inductance that involved in the first kind of cross-coupling with the *k*th coil. Consequently, the suppositional adjacent mutual inductances $M'_{k(k+1)}$ and $M'_{(k+1)k}$ may be unequal.

The second type is the cross-coupling $M_{k(k\pm2a)}$ between the $(k\pm2a)$th coil and the *k*th coil, where $1 \leq k\pm2a \leq n$ and *a* is a positive integer. The current phase of $(k\pm2a)$th coil is either -180° (out of phase) or 0° (in phase) relative to the current phase of *k*th coil, as shown in Fig. 5. This type of cross-coupling can be eliminated by adjusting the compensation capacitor C_k of the *k*th coil.

The compensation capacitance C_k, L_k, and the second type of cross-coupling $M_{k(k\pm 2a)}$ satisfy the relationship in

$$F_{R\_S}(k)+F_{L\_S}(k)+\dot{I}_k\left(j\omega L_k+\frac{1}{j\omega C_k}\right)=0 \tag{14}$$

with

$$F_{R\_S}(k)=\begin{cases}\sum_{a=1}^{\frac{n-k}{2}}\omega^2\cdot M_{k(k+2a)}\cdot\dot{I}_{k+2a} & 1\le k<n-1\\ 0 & n-1\le k\le n\end{cases}$$

$$F_{L\_S}(k)=\begin{cases}\sum_{a=1}^{\frac{k-1}{2}}\omega^2\cdot M_{k(k-2a)}\cdot\dot{I}_{k-2a} & 2<k\le n\\ 0 & 1\le k\le 2\end{cases}.$$

$F_{R\_S}(k)$ represents the sum of induced voltages generated by the second type of cross-coupling coils on the right-side of the coil, and $F_{L\_S}(k)$ represents the sum of induced voltages generated by the second type of cross-coupling coils on the left-side of the coil. However, for the first and second coils, the induced voltage term on the left-side $F_{L\_S}(k)$ is 0, while for the (n-1)th and nth coils, the induced voltage term on the right-side $F_{R\_S}(k)$ is 0. The key distinction between (14) and (4) lies in the resonance formation: the capacitance C_k in (4) only resonates with the self-inductance L_k, whereas the capacitance C_k in (14), in addition to L_k, also resonates with the equivalent impedance reflected from the second type of cross-coupling $M_{k(k\pm 2a)}$ onto the coil.

According to the discussion on the phase relationship of coil currents and the effect of cross-coupling on each coil loop, it can be seen that the coupling between the adjacent coils will naturally eliminate the first type of cross-coupling, while the second type of cross-coupling must be addressed by adjusting the compensation capacitance. Obviously, the purpose of eliminating cross-coupling in the domino WPT system is achieved, as long as the compensation capacitance C_k can be calculated from (14). Thus, C_k can be further expressed as

$$C_k=\frac{\dot{I}_k}{F_{R\_S}(k)+F_{L\_S}(k)+\omega^2\cdot L_k\cdot\dot{I}_k} \tag{15}$$

where the second type of cross-coupling $M_{k(k\pm 2a)}$ and the coil self-inductance L_k are determined by the actual measurement. Moreover, the unknown I_k is solved from (8), where the superpositional mutual inductances $M'_{k(k+1)}$ and $M'_{(k+1)k}$ can be substituted by the first type of cross-coupling $M_{k(k\pm(1+2a))}$ according to (13). So far, the analytical formula for calculating the compensation capacitor C_k is derived. By eliminating cross-coupling in the domino WPT system with SEF path, each coil loop is fully resonant, and ZPA input and CV/CC output characteristics can be fulfilled simultaneously.

III. MEF PATH SYSTEM

A. MEF Path Planning Based on Current Phase Configuration

The method proposed in the SEF path system has successfully eliminated the influence of cross-coupling via the circuit equivalent compensation. The current phase of each coil is configured with 90° of decline gradient, to realize a step-by-step power transmission mode throughout the domino coils. Therefore, if there are several energy flow paths that are all planned according to such phase relationship, the MEF path transmission mode can be formed to meet the needs of multiload power supply in practice.

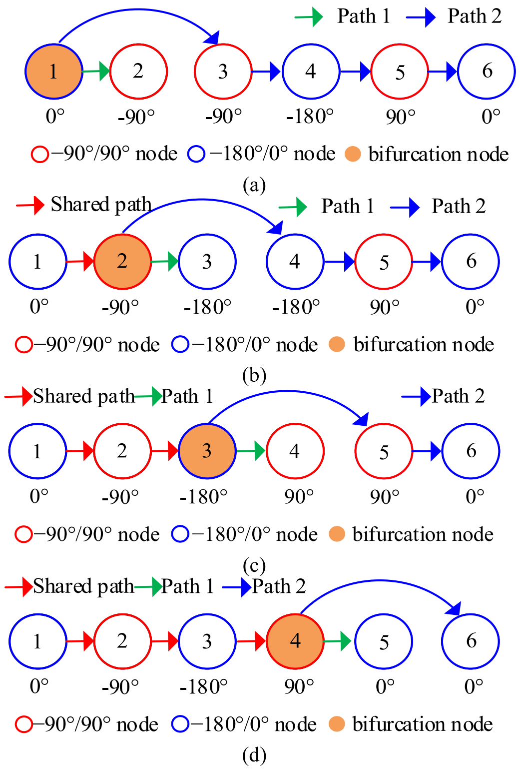

Fig. 6. Dual energy flow paths of six-coil system with (a) bifurcation on the first coil, (b) bifurcation on the second coil, (c) bifurcation on the third coil, and (d) bifurcation on the fourth coil.

First, take the phase of input voltage as the reference 0°, and based on the preplanned energy flow path, the phase relationship among the coil currents is determined. Then, the domino coils can be classified as CV stage coils with the phase of −180°/0° and CC stage coils with the phase of 90°/−90°. Taking the six-coil system as an example, four different dual energy flow paths are constructed. The coil current phase and energy flow paths are shown in Fig. 6.

As shown in Fig. 6, the common coil nodes form a shared path, while the independent coil nodes form path1 and path2 respectively. From the transmitting node to any receiving node, the current phases are periodically arranged according to 0°, -90°, -180°, and 90°. Fig. 6(a) shows a dual energy flow path system where energy flow branches from the first coil. The first, fourth, and sixth coils are CV stage coils, while the second, third, and fifth coils are CC stage coils. Fig. 6(b) shows a dual energy flow path system where energy flow branches from the second coil. The first, third, fourth, and sixth coils are CV stage coils, while the second, and fifth coils are CC stage coils. Fig. 6(c) shows a dual energy flow path system where energy flow branches from the third coil. The first, third, and sixth coils are CV stage coils, while the second, fourth, and fifth coils are CC stage coils. Fig. 6(d) shows a dual energy flow path system where energy flow branches from the fourth coil. The first, third,

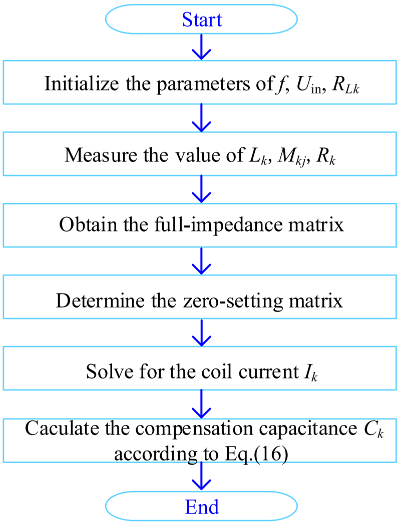

Fig. 7. Calculation flow chart of compensation capacitor C_k.

fifth, and sixth coils are CV stage coils, while the second, and fourth coils are CC stage coils.

It is similar to the SEF path system that the compensation capacitance C_k is the key to achieving the preplanned MEF paths for multiple loads. However, the calculation of the compensation capacitance C_k needs to consider the specific energy flow path distribution. In the light of the previous analysis, the first type of cross-coupling can be directly eliminated by the adjacent mutual inductance, which is also appropriate for the MEF path system because of the phase difference of exactly 90° between the CV stage coil and the CC stage coil. However, the first type of cross-coupling has a great influence on the amplitude of coil currents. The second type of cross-coupling in the MEF path system exits between CV stage coils or between CC stage coils, where the phase difference of coil currents is either -180° or 0°. It can be eliminated by adjusting the compensation capacitance C_k of the coils, and the relationship between the second type of cross-coupling and resonant matching parameters in the coil loop is shown in the following equation:

$$F_{R\_M}(k) + F_{L\_M}(k) + \dot{I}_k\left(j\omega L_k + \frac{1}{j\omega C_k}\right) = 0. \tag{16}$$

In (16), $F_{R\_M}(k)$ represents the sum of induced voltages on the right-side of the coil and $F_{L\_M}(k)$ represents the sum of induced voltages on the left-side of the coil, both of which are caused by the second type of cross-coupling. Different from (14), the specific expressions of $F_{R\_M}(k)$ and $F_{L\_M}(k)$ depend on the configuration of the MEF paths. Therefore, not only the self-inductance L_k, but also the second type of cross-coupling are compensated by the capacitor C_k.

The process of calculating the compensation capacitor C_k is in detail shown in Fig. 7. In order to explain this process, take the dual energy flow path bifurcated from the second coil shown in Fig. 6(b) as an example.

First of all, the circuit parameters such as the operating frequency f, the dc input voltage U_{in}, the dc load on the kth coil R_{Lk}, and the coil parameters such as the self-inductance L_{k}, the mutual inductance M_{kj}, the internal resistance R_{k} are known through the initialization and measurement. According to the specific MEF paths and load ports, the full-impedance matrix that includes all the cross-coupling is obtained as follows:

$$\begin{bmatrix} U_{\text{inv}} \\ 0 \\ 0 \\ 0 \\ 0 \\ 0 \end{bmatrix} = \begin{bmatrix} X_{11} & X_{12} & X_{13} & X_{14} & X_{15} & X_{16} \\ X_{21} & X_{22} & X_{23} & X_{24} & X_{25} & X_{26} \\ X_{31} & X_{32} & X_{33}+R_{Leq3} & X_{34} & X_{35} & X_{36} \\ X_{41} & X_{42} & X_{43} & X_{44} & X_{45} & X_{46} \\ X_{51} & X_{52} & X_{53} & X_{54} & X_{55} & X_{56} \\ X_{61} & X_{62} & X_{63} & X_{64} & X_{65} & X_{66}+R_{Leq6} \end{bmatrix} \cdot \begin{bmatrix} \dot{I}_1 \\ \dot{I}_2 \\ \dot{I}_3 \\ \dot{I}_4 \\ \dot{I}_5 \\ \dot{I}_6 \end{bmatrix}. \tag{17}$$

Here, it can be seen that the third and sixth coils are both receiving coils, so there are two load ports: R_{Leq3} and R_{Leq6} represent the ac equivalent load on the third coil and the sixth coil, respectively. They can be written as

$$R_{Leqk} = \frac{8}{\pi^2} R_{Lk}, k = 3, 6. \tag{18}$$

And the output voltage of the high-frequency inverter has the relationship of

$$U_{\text{inv}} = \frac{2\sqrt{2}}{\pi} U_{\text{in}}. \tag{19}$$

Then, by zeroing the second type of cross-coupling terms and the imaginary part of the diagonal elements, the full-impedance matrix can be transformed into a zero-setting matrix only composed of the first type of cross-coupling terms and the real part of the diagonal elements. For the dual energy flow path system in Fig. 6(b), the zero-setting matrix is as

$$\begin{bmatrix} U_{\text{inv}} \\ 0 \\ 0 \\ 0 \\ 0 \\ 0 \end{bmatrix} = \begin{bmatrix} Z_1 & X_{12} & 0 & 0 & X_{15} & 0 \\ X_{21} & Z_2 & X_{23} & X_{24} & 0 & X_{26} \\ 0 & X_{32} & Z_3 & 0 & X_{35} & 0 \\ 0 & X_{42} & 0 & Z_4 & X_{45} & 0 \\ X_{51} & 0 & X_{53} & X_{54} & Z_5 & X_{56} \\ 0 & X_{62} & 0 & 0 & X_{65} & Z_6 \end{bmatrix} \cdot \begin{bmatrix} \dot{I}_1 \\ \dot{I}_2 \\ \dot{I}_3 \\ \dot{I}_4 \\ \dot{I}_5 \\ \dot{I}_6 \end{bmatrix} \tag{20}$$

where Z_k is denoted by

$$Z_k = \begin{cases} R_k, k = 1, 2, 4, 5 \\ R_k + \frac{8}{\pi^2} R_{Lk}, k = 3, 6 \end{cases}. \tag{21}$$

Despite the existence of the first type of cross-coupling in the zero-setting matrix, the adjacent mutual inductance can automatically eliminate their influence. Therefore, the zero-setting matrix has another equivalent representation by using the suppositional mutual inductances that is

$$\begin{bmatrix} U_{\text{inv}} \\ 0 \\ 0 \\ 0 \\ 0 \\ 0 \end{bmatrix} = \begin{bmatrix} Z_1 & X'_{12} & 0 & 0 & 0 & 0 \\ X'_{21} & Z_2 & X'_{23} & X'_{24} & 0 & 0 \\ 0 & X'_{32} & Z_3 & 0 & 0 & 0 \\ 0 & X'_{42} & 0 & Z_4 & X'_{45} & 0 \\ 0 & 0 & 0 & X'_{54} & Z_5 & X'_{56} \\ 0 & 0 & 0 & 0 & X'_{65} & Z_6 \end{bmatrix} \cdot \begin{bmatrix} \dot{I}_1 \\ \dot{I}_2 \\ \dot{I}_3 \\ \dot{I}_4 \\ \dot{I}_5 \\ \dot{I}_6 \end{bmatrix}. \tag{22}$$

The current magnitude I_k of each coil can be calculated based on the zero-setting impedance matrix that has kept away from all the coil-coupling influence. Finally, according to (16), the value of compensation capacitance C_k is calculated as

$$\begin{aligned} C_1 &= \frac{j \cdot \dot{I}_1}{\dot{I}_1 \cdot \omega^2 \cdot j \cdot L_1 + \omega \cdot \left(\dot{I}_3 \cdot X_{13} + \dot{I}_4 \cdot X_{14} + \dot{I}_6 \cdot X_{16}\right)} \\ C_2 &= \frac{j \cdot \dot{I}_2}{\dot{I}_2 \cdot \omega^2 \cdot j \cdot L_2 + \omega \cdot \dot{I}_5 \cdot X_{25}} \\ C_3 &= \frac{j \cdot \dot{I}_3}{\dot{I}_3 \cdot \omega^2 \cdot j \cdot L_3 + \omega \cdot \left(\dot{I}_1 \cdot X_{31} + \dot{I}_4 \cdot X_{34} + \dot{I}_6 \cdot X_{36}\right)} \\ C_4 &= \frac{j \cdot \dot{I}_4}{\dot{I}_4 \cdot \omega^2 \cdot j \cdot L_4 + \omega \cdot \left(\dot{I}_3 \cdot X_{43} + \dot{I}_1 \cdot X_{41} + \dot{I}_6 \cdot X_{46}\right)} \\ C_5 &= \frac{j \cdot \dot{I}_5}{\dot{I}_5 \cdot \omega^2 \cdot j \cdot L_5 + \omega \cdot \dot{I}_2 \cdot X_{52}} \\ C_6 &= \frac{j \cdot \dot{I}_6}{\dot{I}_6 \cdot \omega^2 \cdot j \cdot L_6 + \omega \cdot \left(\dot{I}_3 \cdot X_{63} + \dot{I}_4 \cdot X_{64} + \dot{I}_1 \cdot X_{61}\right)}. \end{aligned} \tag{23}$$

Because the phase difference of the currents in (23) is either 0° or 180°, *j* can be canceled out and C_k is a real number. The other formulas for C_k calculating can be found in Appendix.

B. Output Characteristics of MEF Path System

Based on the previous analysis, the number of coils in the SEF path system can be adjusted to achieve single-load CV/CC output. However, the relationship between multiload CV outputs and the energy flow paths remains unclear. Taking the four energy flow paths in Fig. 6 as an example, the realization conditions of multiload CV outputs of the system are analyzed and discussed. The system circuit parameters are shown in Table I.

TABLE I
CIRCUIT PARAMETERS OF SIX-COIL SYSTEM IN SIMULATION

Symbols	Parameter	Value	Unit
f	frequency	500	kHz
U_{in}	DC input	30	V
L_1~L_6	self-inductance	19.023/19.297/22.442/22.533/ 25.638/25.234	μH
R_1–R_6	ESR of coils	0.16/0.154/0.157/0.147/ 0.156/0.163	Ω
$M_{12}/M_{23}/M_{34}/M_{45}/M_{56}$	mutual inductance	2.879/3.095/3.738/3.799/3.852	μH
$M_{13}/M_{24}/M_{35}/M_{46}/M_{14}$		0.931/0.988/0.239/0.42/0.25	μH
$M_{25}/M_{36}/ M_{15}/M_{26}/M_{16}$		0.29/0.59/0.361/0.325/0.141	μH
C_1~C_6	Compensation capacitor in the first energy flow path	5.5137/5.4055/2.4753/4.9451/ 4.1526/4.1876	nF
C_1~C_6	Compensation capacitor in the second energy flow path	5.8264/3.2009/3.0371/4.4604/ 4.1529/4.1733	nF
C_1~C_6	Compensation capacitor in the third energy flow path	6.136/6.0335/5.2658/5.3655/ 0.4506/4.0802	nF
C_1~C_6	Compensation capacitor in the fourth energy flow path	6.2904/6.033/5.3038/5.3757/ 4.0001/2.5371	nF

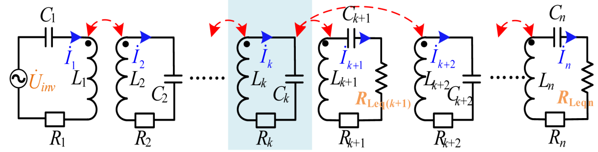

Fig. 8. Dual energy flow paths system with bifurcation on the *k*th coil.

In a dual energy flow path system, assume the *k*th coil serves as a bifurcation node and the (*k*+1)th coil serves as one of the output ports. Then the (*k*+2)th coil will skip the (*k*+1)th coil and couple directly with the *k*th coil to achieve the energy flow splitting, as shown in Fig. 8. The impedances of these three coil loops are as

$$\begin{aligned} Z_{k+2} &= X_{k+2} + R_{\text{eq}(k+2)} \\ &= R_{k+2} + j\left(\omega L_{k+2} - 1/\omega C_{k+2}\right) + R_{\text{eq}(k+2)} \end{aligned} \tag{24}$$

$$\begin{aligned} Z_{k+1} &= X_{k+1} + R_{L\text{eq}(k+1)} \\ &= R_{k+1} + j\left(\omega L_{k+1} - 1/\omega C_{k+1}\right) + R_{L\text{eq}(k+1)} \end{aligned} \tag{25}$$

$$\begin{aligned} Z_k &= X_k + R_{\text{eq}k} \\ &= R_k + j\left(\omega L_k - 1/\omega C_k\right) + R_{\text{eq}k} \end{aligned} \tag{26}$$

where

$$\begin{aligned} R_{\text{eq}(k+2)} &= \frac{\omega^2 \cdot M'_{(k+2)(k+3)} \cdot M'_{(k+3)(k+2)}}{Z_{k+3}} \\ R_{L\text{eq}(k+1)} &= \frac{8}{\pi^2} R_{L(k+1)} \\ R_{\text{eq}k} &= \frac{\omega^2 \cdot M'_{k(k+1)} \cdot M'_{(k+1)k}}{Z_{k+1}} \\ &\quad + \frac{\omega^2 \cdot M'_{k(k+2)} \cdot M'_{(k+2)k}}{Z_{k+2}}. \end{aligned}$$

By combining the current expression in (8), the expressions of output voltage and output current in the four energy flow paths are derived, as shown in Table V, which can be found in Appendix. It is known that the CV output can be achieved in the cases of Fig. 6(b) and (d), while the load-independent constant output cannot be achieved in the cases of Fig. 6(a) and (c).

TABLE II
CIRCUIT PARAMETERS OF SEVEN COIL PROTOTYPE SYSTEM

Symbols	Parameter	Value	Unit
f	frequency	200	kHz
U_{in}	DC input	35	V
L_1~L_7	self-inductance	171.21/172.49/172.99/173.01/173.13/171.58/171.91	μH
R_1~R_7	ESR of coils	0.434/0.437/0.456/0.434/0.432/0.49/0.428	Ω
$M_{12}/M_{23}/M_{34}/M_{45}/M_{56}/M_{67}$	mutual inductance	28.54/28.095/28.175/29.065/28.782/28.288	μH
$M_{13}/M_{24}/M_{35}/M_{46}/M_{57}$		8.23/8.148/8.41/8.408/8.403	μH
$M_{14}/M_{25}/M_{36}/M_{47}$		3.088/3.185/3.173/3.208	μH
$M_{15}/M_{26}/M_{37}/M_{16}$		1.593/1.473/1.490/0.765	μH
M_{27}/M_{17}		0.793/0.399	μH
C_1~C_7	compensation capacitor	3.873/3.837/3.989/4.00/4.00/3.867/3.861	nF

TABLE III
CIRCUIT PARAMETERS OF SIX COIL PROTOTYPE SYSTEM

Symbols	Parameters	Value	Unit
f	frequency	500	kHz
U_{in}	DC input	30	V
L_1~L_6	self-inductance	19.023/19.297/22.442/22.533/25.638/25.234	μH
R_1~R_6	ESR of coils	0.16/0.154/0.157/0.147/0.156/0.163	Ω
$M_{12}/M_{23}/M_{34}/M_{45}/M_{56}$	mutual inductance	2.879/16.238/3.738/3.799/3.852	μH
$M_{13}/M_{24}/M_{35}/M_{46}/M_{14}$		2.827/3.037/1.192/1.046/0.931	μH
M_{25}/M_{36} /$M_{15}/M_{26}/M_{16}$		0.988/0.239/0.361/0.325/0.141	μH
L_{c}	compensating inductor	13.143	μH
R_{Lc}	ESR of L_{c}	0.170	Ω
C_1~C_6	compensation capacitor	5.80/3.20/3.06/4.48/4.15/4.17	nF

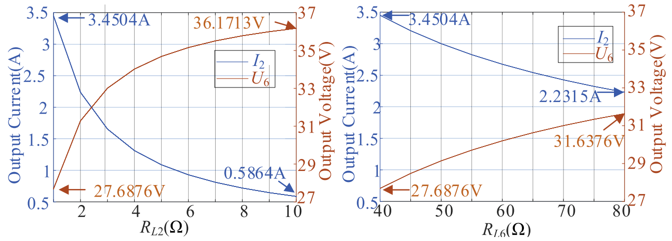

(a) (b)

Fig. 9. Dual outputs system bifurcated on the first coil. (a) $R_{L6} = 40\,\Omega$. (b) $R_{L2} = 1\,\Omega$.

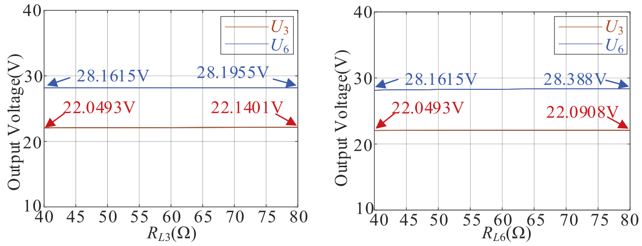

(a) (b)

Fig. 10. Dual outputs system bifurcated from the second coil. (a) $R_{L6} = 40\ \Omega$. (b) $R_{L3} = 40\ \Omega$.

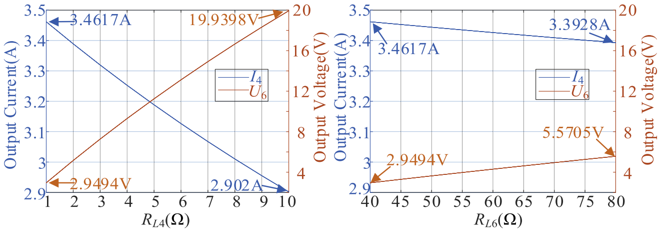

(a) (b)

Fig. 11. Dual outputs system bifurcated from the third coil. (a) $R_{L6} = 40\,\Omega$. (b) $R_{L4} = 1\,\Omega$.

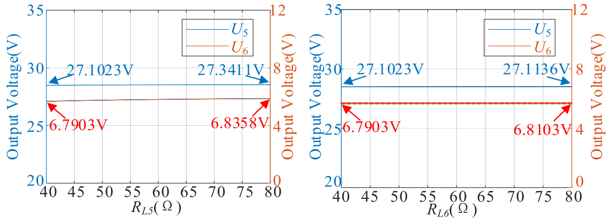

(a) (b)

Fig. 12. Dual outputs system bifurcated from the fourth coil. (a) $R_{L6} = 40\,\Omega$. (b) $R_{L5} = 40\,\Omega$.

The multiload output characteristics of the six-coil system are shown from Figs. 9–12. Fig. 9 illustrates the output characteristics of the system with energy flow branching from the first coil. R_{L2} and R_{L6} represent the dc loads on the second and sixth coils, respectively. From the figure, it can be seen that this system cannot achieve the load-independent CV output. Fig. 10 shows the output characteristics of the system with energy flow branching from the second coil. R_{L3} and R_{L6} represent the dc loads on the third and sixth coils, respectively. This system can achieve the load-independent CV output. Fig. 11 shows the output characteristics of the system with energy flow branching from the third coil. R_{L4} and R_{L6} represent the dc loads on the fourth and sixth coils, respectively. This system cannot achieve the load-independent CV output. Fig. 12 shows the output characteristics of the system with energy flow branching from the fourth coil. R_{L5} and R_{L6} represent the dc loads on the fifth and sixth coils, respectively. This system can achieve the load-independent CV output.

By comparing Fig. 10 (see Fig. 12) with Fig. 9 (see Fig. 11), it is evident that the MEF path system with bifurcation from the CC stage coil can achieve the multiload CV outputs. This is because the current of the CC stage coil is independent of the load. In contrast, when the bifurcation node is a CV stage coil, the coil current is affected by the load. The experimental results are consistent with the previous theoretical analysis shown in Table V. Therefore, in order to achieve a multiload CV outputs in the domino WPT system, it is necessary to construct such MEF paths whose energy flow can be bifurcated on the CC stage coils. In addition, for the receiving node of the energy flow path, the node type should be a CV stage coil.

TABLE IV
COMPARISON WITH SIMILAR WORKS ABOUT MULTILOAD IN RECENT YEARS

	[11]	[25]	[26]	[27]	[32]	This Work
Air Gap Between Adjacent Coils	40 cm	6 cm	3 cm	5 cm	6 cm	8.33 cm
DC-DC Efficiency	66.7%	/	/	/	63.7%	79.68%
Voltage/Current Variation Ratio	<5%	<20%	<15%	>12.07%	<10%	<5%
Load-Independent Outputs	YES	YES	YES	YES	YES	YES
Number of Coils	8	21	14	13	13	6
Coil Type	CSC	Planar	Planar	Planar	Planar	Planar
Total Distance	2.5 m	0.6 m	0.18 m	0.2 m	0.36 m	0.33 m
Total Load Power	20.32 W	30 W	14.64 W	22 W	23.93 W	37.41 W
CC/CV	CV	CC	CC	CV	CV	CV
Ferrite Plate	YES	YES	YES	YES	YES	NO
Compensation Network	S	S/T	LCC	S-CLC	S/LCC	S/CLC
Special Coil Structure	NO	DD	DD	DD	DD	NO

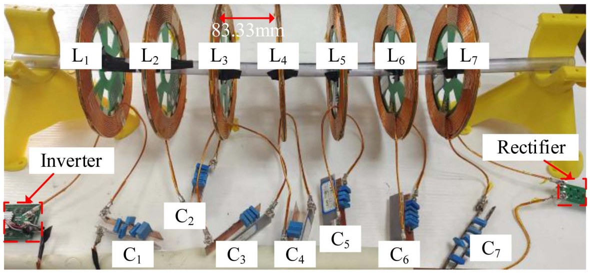

Fig. 13. Seven-coil experimental prototype.

IV. EXPERIMENTAL VERIFICATION

The prototypes of seven-coil domino system and six-coil domino system are constructed respectively to verify the method proposed in this article. By setting the SEF path in the seven-coil system, the single load CV output is tested, and then the multiload CV outputs of the six-coil system are also evaluated with the configuration of dual energy flow paths.

A. Single Load CV Output

For the seven-coil system shown in Fig. 13, the diameter of each coil is 200 mm, with an adjacent coil spacing of 83.33 mm. The input dc voltage of the prototype is 35 V, and the output power is controlled through the variations in dc load. The load resistance is varied from 45 Ω to 135 Ω. The mutual inductance and self-inductance parameters of the coils are listed in Table II. All waveforms are recorded by an Agilent DSO-X3034A oscilloscope.

The steady-state waveforms of the seven-loop currents and input voltage are illustrated in Fig. 14. The first loop current I_1 is almost in phase with the input voltage U_{inv}, indicating that the ZPA condition is realized. The phase differences between adjacent currents are measured as 85.14°, 88.2°, 83.53°, and 84.32°, respectively. In addition, the magnitudes of I_2, I_4, and I_6 are slightly larger than those of I_1, I_3, I_5, and I_7.

To verify the CV characteristics of the seven-coil system, the transient waveforms of the DC output voltage U_{out}, the first loop current $I_{1,}$ and the seventh loop current I_7 are shown in Fig. 15. These waveforms are observed at different load conditions, with R_L varying from 45 Ω to 90 Ω and from 45 Ω to 135Ω.

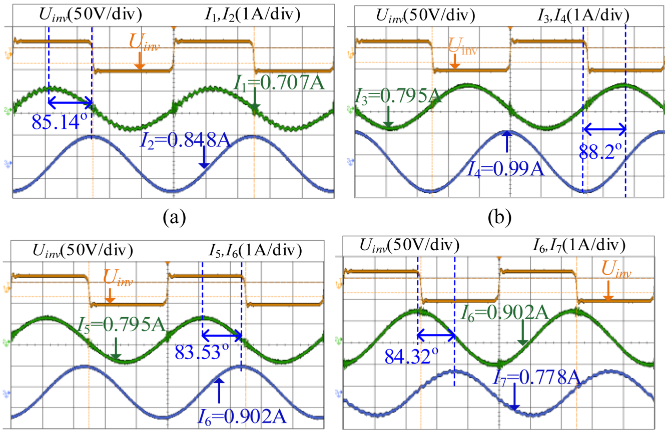

(a) (b)

(c) (d)

Fig. 14. Steady-state waveforms of seven-coil system. (a) I_1, I_2, and U_{inv}. (b) I_3, I_4, and U_{inv}. (c) I_5, I_6, and U_{inv}. (d) I_6, I_7, and U_{inv}.

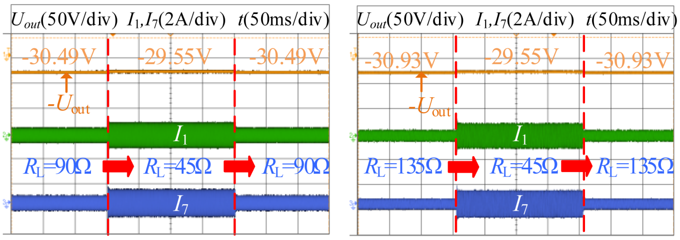

(a) (b)

Fig. 15. Transient waveforms of seven-coil system with (a) R_L varying from 45 Ω to 90 Ω. (b) R_L varying from 45 Ω to 135 Ω.

The voltage change rate is defined as $(U – U_r)/U_r$, where U and U_r are the output voltages under a certain dc load (such as 90 Ω or 135 Ω) and rated dc load (45 Ω), respectively. As shown in Fig. 15(a), when the load changes from 45 Ω to 90 Ω, the load voltage changes from 29.55 V to 30.49 V. As shown in Fig. 15(b), when the load changes from 45 Ω to 135 Ω, the load voltage changes from 29.55 V to 30.93 V. In both cases, the voltage change rate remains within 5%, indicating that the CV characteristics are successfully achieved.

The experimental efficiency of the seven-coil system from dc power supply to dc load is presented in Fig. 16. The maximum

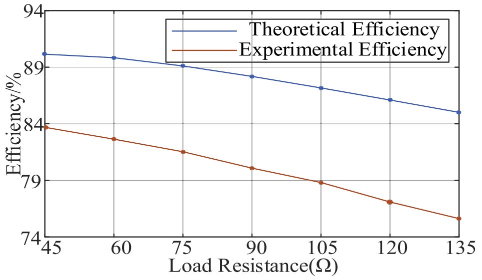

Fig. 16. Theoretical and experimental efficiency of seven-coil system.

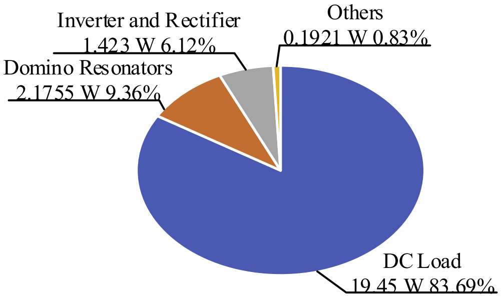

Fig. 17. Power distribution of seven-coil system at $R_L = 45\,\Omega$.

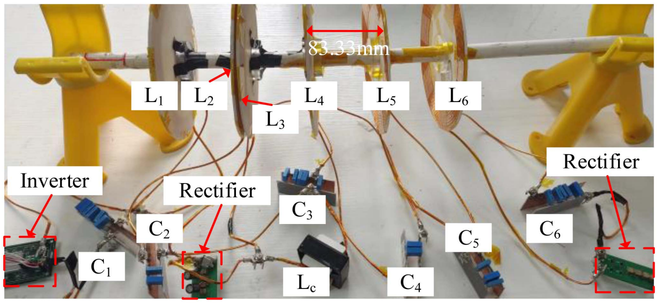

Fig. 18. Six-coil experimental prototype.

experimental efficiency of the system reaches 83.69% at the load of 45 Ω. And the power distribution at the load of 45 Ω is shown in Fig. 17. Obviously, in the CV mode, the losses of the domino resonators and switching account for the majority of the total system loss. In addition, Fig. 16 shows the theoretical efficiency calculated in (12), which does not take into account the inverter and rectifier losses. Therefore, a noticeable difference is found between the theoretical and experimental efficiency, and it is approximately equal to the inverter and rectifier losses.

B. Multiload CV Outputs

For the six-coil system shown in Fig. 18, the diameter of each coil is 200 mm and the spacing between adjacent coils is 83.33 mm, except for the spacing between the third and second coils, which is 4 mm. Unlike the seven-coil system where all the coils are equally spaced, the six-coil system places the second and third coils close to each other. This is because the mutual inductance M_{24} is too small with an equally spaced arrangement, resulting in a large difference between the output voltages of two loads. However, excessive mutual inductance M_{23} occurs after placing the second and third coils close to each other, also leading to a large voltage difference between the two loads when using S compensation topology in Fig. 19(a). To balance the voltage outputs, a CLC compensation topology is thus used to connect the second coil and the third coil, while the other coils still use the S compensation topology, as shown in Fig. 19(b). The prototype operates with an input dc voltage of 30 V, and the output power is influenced by a variable dc load that ranges from 40 Ω to 80 Ω. Detailed parameters for mutual inductance and self-inductance of the coils are provided in Table III. In addition, the parasitic capacitance between the compensation capacitors and its effect can be neglected.

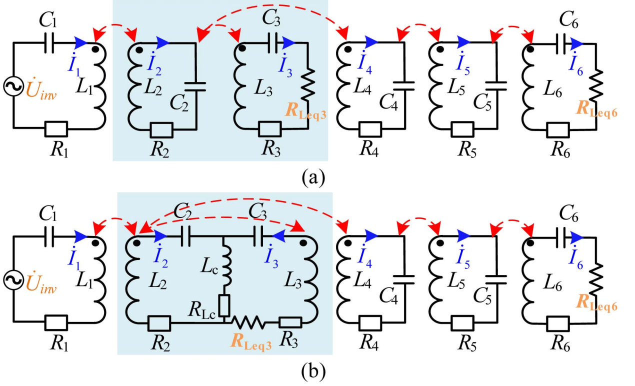

Fig. 19. Coils L_2 and L_3 in close proximity arrangement with (a) S compensation topology and (b) CLC compensation topology.

The effect of the introduced CLC compensation topology on the six-coil system is equivalent to weakening the mutual impedance between L_2 and L_3 and meanwhile increasing the self-impedance of L_2 and L_3. Thus, the output voltages of U_3 and U_6 in CLC compensation are as

$$U_3 = \frac{(M'_{32} - L_c)\, U_{\text{inv}}}{M'_{12}} \tag{27}$$

$$U_6 = \frac{M'_{42} M'_{65} U_{\text{inv}}}{M'_{12} M'_{45}}. \tag{28}$$

By adjusting the value of L_c, the CLC compensation topology can effectively balance the output voltages between different load-ports and significantly reduce the voltage fluctuations with load changes in the dual energy flow path system.

The steady-state waveforms of the six-loop currents and input voltage are shown in Fig. 20. The first loop current I_1 is almost in phase with the input voltage U_{inv}, confirming the realization of the ZPA condition. As discussed in the previous analysis, in addition to I_3 and I_4 being in phase, the phase difference between the adjacent coils is approximately 90°.

To verify the multioutput CV characteristics of the six-coil system, the transient waveforms of dc output voltage U_3 and U_6, the third loop current I_3, and the sixth loop current I_6 are illustrated in Fig. 21. As illustrated in Fig. 21(a), when R_{L6} is constant and R_{L3} changes from 40 Ω to 80 Ω, the load voltage

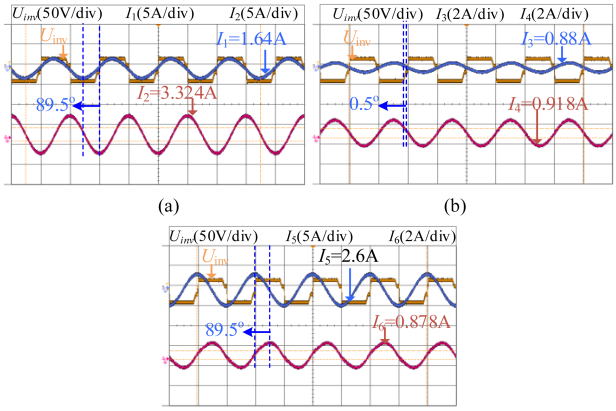

(a) (b)

(c)

Fig. 20. Steady-state waveforms of six-coil system. (a) I_1, I_2, and U_{inv}. (b) I_3, I_4, and U_{inv}. (c) I_5, I_6, and U_{inv}.

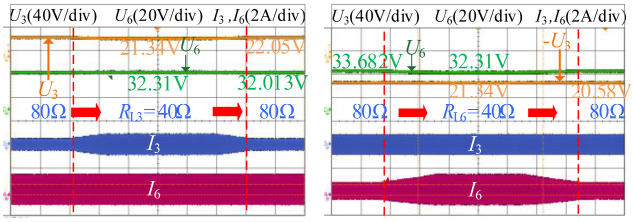

(a) (b)

Fig. 21. Transient waveforms of six-coil system with (a) $R_{L6} = 40\,\Omega$, R_{L3} changing from $40\,\Omega$ to $80\,\Omega$ and (b) $R_{L3} = 40\,\Omega$, R_{L6} changing from $40\,\Omega$ to $80\,\Omega$.

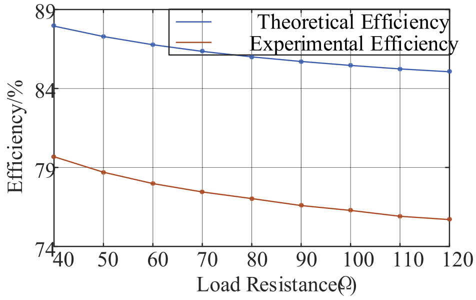

Fig. 22. Theoretical and experimental efficiency of the six-coil system.

U_3 varies from 21.34 V to 22.05 V, while the load voltage U_6 changes from 32.31 V to 32.013 V. As shown in Fig. 21(b), when R_{L3} is constant and R_{L6} changes from $40\,\Omega$ to $80\,\Omega$, the load voltage U_6 varies from 32.31 V to 33.682 V, while the load voltage U_3 changes from 21.34 V to 20.58 V. In both cases, the voltage change rate remains within 5%, confirming the multioutput CV characteristic, and the load isolation is achieved when one load changes and the other load voltage changes less than 5%.

The experimental efficiency of the six-coil system from dc power supply to dc load is measured with the change of load, as shown in Fig. 22. The maximum experimental efficiency of the system achieves 79.68%. Due to the switching losses in the inverter and rectifier, the experimental efficiency is lower than the theoretical efficiency that can be calculated by

$$\eta = \frac{I_6^2 R_{\text{Leq6}} + I_3^2 R_{\text{Leq3}}}{U_{\text{inv}} I_1} = \frac{8}{\pi^2} \frac{I_6^2 R_{\text{L6}} + I_3^2 R_{\text{L3}}}{U_{\text{inv}} I_1}. \tag{29}$$

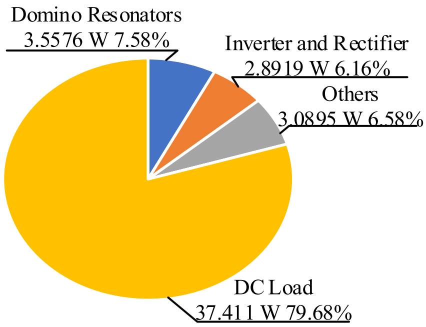

Fig. 23. Power distribution of six-coil system when R_{L3} and R_{L6} are both $40\,\Omega$.

The power distribution when R_{L3} and R_{L6} are both $40\,\Omega$ is shown in Fig. 23. In the multiload CV mode, the losses of domino resonators, inverter, and rectifier are 3.5576 W and 2.8919 W, respectively, accounting for 7.58% and 6.16% of the total loss. Due to the compensation inductance L_c, an additional loss of 2.0088 W is introduced, so that the power ratio of Others increases, accounting for 6.58% of the total power. Therefore, the domino resonators, compensation inductance, inverter, and rectifier are the main factors affecting the system efficiency.

In recent years, research on multiload WPT system has been analyzed in [11], [25], [26], [27], and [32]. The comparison between the system proposed in this article and other existing systems is shown in Table IV. Compared to other systems, the proposed system does not require ferromagnetic materials, thereby reducing the overall weight and volume of the system. In addition, it avoids specialized coil configurations such as DDQ and orthogonal DD, which broadens the applicable coil shapes and simplifies system design. This article uses a relatively simple compensation network to achieve a CV output characteristic with multiple load independence, reducing the number of reactive components and simplifying the system.

V. CONCLUSION

This article proposes a domino WPT energy flow path planning method based on the current phase configuration. The system energy flow path can be planned by adjusting the compensation capacitors of each coil without altering the coil structure. A detailed flowchart for capacitor parameter design is provided, and the relationship between the energy flow path and system output characteristics is analyzed. It is concluded that the MEF paths with energy flow branching from the CC stage coils should be constructed for multiload CV outputs. The effectiveness and accuracy of the proposed method are verified via the experiment. Prototypes of the seven-coil domino system and six-coil domino system are constructed, and experimental results show that the seven-coil SEF path system achieves CV output for a single load and the six-coil MEF system achieves CV output for dual loads. In conclusion, this article offers a

TABLE V
OUTPUT EXPRESSIONS FOR DIFFERENT MEF PATHS OF SIX-COIL SYSTEM

Cases	Voltage at output port 1	Current at output port 1	Voltage at output port 2	Current at output port 2
case1	$U_2=\dfrac{\omega M'_{21}U_{inv}R_{eq2}}{\dfrac{M'_{13}M'_{31}R_{eq2}M'_{45}M'_{54}R_{eq6}}{M'_{56}M'_{65}M'_{34}M'_{43}}+\omega^2M'_{12}M'_{21}}$	$I_2=\dfrac{\omega M'_{21}U_{inv}}{\dfrac{M'_{13}M'_{31}R_{eq2}M'_{45}M'_{54}R_{eq6}}{M'_{56}M'_{65}M'_{34}M'_{43}}+\omega^2M'_{12}M'_{21}}$	$U_6=\dfrac{R_{eq2}M'_{31}U_{inv}M'_{43}M'_{65}}{\left(M'_{13}M'_{31}R_{eq2}+M'_{12}M'_{21}\dfrac{\omega^2M'_{56}M'_{65}M'_{34}M'_{43}}{M'_{45}M'_{54}R_{eq6}}\right)M'_{45}}$	$I_6=\dfrac{R_{eq2}M'_{31}U_{inv}M'_{43}M'_{65}}{\left(M'_{13}M'_{31}R_{eq2}+M'_{12}M'_{21}\dfrac{M'_{56}M'_{65}M'_{34}M'_{43}\omega^2}{M'_{45}M'_{54}R_{eq6}}\right)M'_{45}R_{eq6}}$
case2	$U_3=\dfrac{M'_{32}U_{inv}}{M'_{12}}$	$I_3=\dfrac{M'_{32}U_{inv}}{M'_{12}R_{eq3}}$	$U_6=\dfrac{M'_{42}M'_{65}U_{inv}}{M'_{12}M'_{45}}$	$I_6=\dfrac{M'_{42}M'_{65}U_{inv}}{M'_{12}M'_{45}R_{eq6}}$
case3	$U_4=\dfrac{\omega^2U_{inv}M'_{32}M'_{43}R_{eq4}}{\omega M'_{12}\left(\dfrac{M'_{35}M'_{53}R_{eq4}R_{eq6}}{M'_{56}M'_{65}}+\omega^2M'_{34}M'_{43}\right)}$	$I_4=\dfrac{\omega^2U_{inv}M'_{32}M'_{43}}{\omega M'_{12}\left(\dfrac{M'_{35}M'_{53}R_{eq4}R_{eq6}}{M'_{56}M'_{65}}+\omega^2M'_{34}M'_{43}\right)}$	$U_6=\dfrac{U_{inv}M'_{32}R_{eq4}\dfrac{M'_{56}M'_{65}}{R_{eq6}}M'_{53}R_{eq6}}{M'_{12}M'_{56}\left(M'_{35}M'_{53}R_{eq4}+M'_{34}M'_{43}\dfrac{\omega^2M'_{56}M'_{65}}{R_{eq6}}\right)}$	$I_6=\dfrac{U_{inv}M'_{32}R_{eq4}\dfrac{M'_{56}M'_{65}}{R_{eq6}}M'_{53}}{M'_{12}M'_{56}\left(M'_{35}M'_{53}R_{eq4}+M'_{34}M'_{43}\dfrac{\omega^2M'_{56}M'_{65}}{R_{eq6}}\right)}$
case4	$U_5=\dfrac{U_{inv}M'_{32}M'_{54}}{M'_{12}M'_{34}}$	$I_5=\dfrac{U_{inv}M'_{32}M'_{54}}{M'_{12}M'_{34}R_{eq5}}$	$U_6=\dfrac{U_{inv}M'_{32}M'_{64}}{M'_{12}M'_{34}}$	$I_6=\dfrac{U_{inv}M'_{32}M'_{64}}{M'_{12}M'_{34}R_{eq6}}$

general calculation method of compensation capacitors to make a good resonance matching with the domino coils, and addresses the challenge to achieve the constant output of multiple loads by planning the energy flow path.

APPENDIX

A. Calculation of Compensation Capacitors When Energy Flow Bifurcated From the First Coil

For the MEF paths in Fig. 6(a), it can be seen that the second and sixth nodes are the receiving coils. According to the calculation flow chart in Fig. 7, the zero-setting matrix can be obtained as

$$\begin{bmatrix} U_{inv} \\ 0 \\ 0 \\ 0 \\ 0 \\ 0 \end{bmatrix} = \begin{bmatrix} Z_1 & X_{12} & X_{13} & 0 & X_{15} & 0 \\ X_{21} & Z_2 & 0 & X_{24} & 0 & X_{26} \\ X_{31} & 0 & Z_3 & X_{34} & 0 & X_{36} \\ 0 & X_{42} & X_{43} & Z_4 & X_{45} & 0 \\ X_{51} & 0 & 0 & X_{54} & Z_5 & X_{56} \\ 0 & X_{62} & X_{63} & 0 & X_{65} & Z_6 \end{bmatrix} \cdot \begin{bmatrix} \dot{I}_1 \\ \dot{I}_2 \\ \dot{I}_3 \\ \dot{I}_4 \\ \dot{I}_5 \\ \dot{I}_6 \end{bmatrix} \tag{30}$$

where Z$_k$ is denoted by

$$Z_k = \begin{cases} R_k, k = 1,3,4,5 \\ R_k + \frac{8}{\pi^2} R_{Lk}, k = 2,6 \end{cases}. \tag{31}$$

According to the zero-setting matrix, the coil currents are solved. By substituting the coil currents into (16), the analytical formula of the compensation capacitor is obtained as

$$C_1 = \frac{j \cdot \dot{I}_1}{\dot{I}_1 \cdot \omega^2 \cdot j \cdot L_1 + \omega \cdot \left(\dot{I}_4 \cdot X_{14} + \dot{I}_6 \cdot X_{16}\right)}$$

$$C_2 = \frac{j \cdot \dot{I}_2}{\dot{I}_2 \cdot \omega^2 \cdot j \cdot L_2 + \omega \cdot \left(\dot{I}_3 \cdot X_{23} + \dot{I}_5 \cdot X_{25}\right)}$$

$$C_3 = \frac{j \cdot \dot{I}_3}{\dot{I}_3 \cdot \omega^2 \cdot j \cdot L_3 + \omega \cdot \left(\dot{I}_2 \cdot X_{32} + \dot{I}_5 \cdot X_{35}\right)}$$

$$C_4 = \frac{j \cdot \dot{I}_4}{\dot{I}_4 \cdot \omega^2 \cdot j \cdot L_4 + \omega \cdot \left(\dot{I}_1 \cdot X_{41} + \dot{I}_6 \cdot X_{46}\right)}$$

$$C_5 = \frac{j \cdot \dot{I}_5}{\dot{I}_5 \cdot \omega^2 \cdot j \cdot L_5 + \omega \cdot \left(\dot{I}_2 \cdot X_{52} + \dot{I}_3 \cdot X_{53}\right)}$$

$$C_6 = \frac{j \cdot \dot{I}_6}{\dot{I}_6 \cdot \omega^2 \cdot j \cdot L_6 + \omega \cdot \left(\dot{I}_1 \cdot X_{61} + \dot{I}_4 \cdot X_{64}\right)}. \tag{32}$$

B. Calculation of Compensation Capacitors When Energy Flow Bifurcated From the Third Coil

For the MEF paths in Fig. 6(c), it can be seen that the fourth and sixth nodes are the receiving coils. According to the calculation flow chart in Fig. 7, the zero-setting matrix can be obtained as

$$\begin{bmatrix} U_{inv} \\ 0 \\ 0 \\ 0 \\ 0 \\ 0 \end{bmatrix} = \begin{bmatrix} Z_1 & X_{12} & 0 & X_{14} & X_{15} & 0 \\ X_{21} & Z_2 & X_{23} & 0 & 0 & X_{26} \\ 0 & X_{32} & Z_3 & X_{34} & X_{35} & 0 \\ X_{41} & 0 & X_{43} & Z_4 & 0 & X_{46} \\ X_{51} & 0 & X_{53} & 0 & Z_5 & X_{56} \\ 0 & X_{62} & 0 & X_{64} & X_{65} & Z_6 \end{bmatrix} \cdot \begin{bmatrix} \dot{I}_1 \\ \dot{I}_2 \\ \dot{I}_3 \\ \dot{I}_4 \\ \dot{I}_5 \\ \dot{I}_6 \end{bmatrix} \tag{33}$$

where Z$_k$ is denoted by

$$Z_k = \begin{cases} R_k, k = 1,2,3,5 \\ R_k + \frac{8}{\pi^2} R_{Lk}, k = 4,6 \end{cases}. \tag{34}$$

According to the zero-setting matrix, the coil currents are solved. By substituting the coil currents into (16), the analytical formula of the compensation capacitor is obtained as

$$C_1 = \frac{j \cdot \dot{I}_1}{\dot{I}_1 \cdot \omega^2 \cdot j \cdot L_1 + \omega \cdot \left(\dot{I}_3 \cdot X_{13} + \dot{I}_6 \cdot X_{16}\right)}$$

$$C_2 = \frac{j \cdot \dot{I}_2}{\dot{I}_2 \cdot \omega^2 \cdot j \cdot L_2 + \omega \cdot \left(\dot{I}_4 \cdot X_{24} + \dot{I}_5 \cdot X_{25}\right)}$$

$$C_3 = \frac{j \cdot \dot{I}_3}{\dot{I}_3 \cdot \omega^2 \cdot j \cdot L_3 + \omega \cdot \left(\dot{I}_1 \cdot X_{31} + \dot{I}_6 \cdot X_{36}\right)}$$

$$C_4 = \frac{j \cdot \dot{I}_4}{\dot{I}_4 \cdot \omega^2 \cdot j \cdot L_4 + \omega \cdot \left(\dot{I}_2 \cdot X_{42} + \dot{I}_5 \cdot X_{45}\right)}$$

$$C_5 = \frac{j \cdot \dot{I}_5}{\dot{I}_5 \cdot \omega^2 \cdot j \cdot L_5 + \omega \cdot \left(\dot{I}_2 \cdot X_{52} + \dot{I}_4 \cdot X_{54}\right)}$$

$$C_6 = \frac{j \cdot \dot{I}_6}{\dot{I}_6 \cdot \omega^2 \cdot j \cdot L_6 + \omega \cdot \left(\dot{I}_1 \cdot X_{61} + \dot{I}_3 \cdot X_{63}\right)}. \tag{35}$$

C. Calculation of Compensation Capacitors When Energy Flow Bifurcated From the Fourth Coil

For the MEF paths in Fig. 6(d), it can be seen that the fifth and sixth nodes are the receiving coils. According to the calculation flow chart in Fig. 7, the zero-setting matrix can be obtained as

$$\begin{bmatrix} U_{inv} \\ 0 \\ 0 \\ 0 \\ 0 \\ 0 \end{bmatrix} = \begin{bmatrix} Z_1 & 0 & X_{13} & 0 & X_{15} & X_{16} \\ 0 & Z_2 & 0 & X_{24} & 0 & 0 \\ X_{31} & 0 & Z_3 & 0 & X_{35} & X_{36} \\ 0 & X_{42} & 0 & Z_4 & 0 & 0 \\ X_{51} & 0 & X_{53} & 0 & Z_5 & X_{56} \\ X_{61} & 0 & X_{63} & 0 & X_{65} & Z_6 \end{bmatrix} \cdot \begin{bmatrix} \dot{I}_1 \\ \dot{I}_2 \\ \dot{I}_3 \\ \dot{I}_4 \\ \dot{I}_5 \\ \dot{I}_6 \end{bmatrix} \tag{36}$$

where Z_k is denoted by

$$Z_k = \begin{cases} R_k, k = 1, 2, 3, 4 \\ R_k + \frac{8}{\pi^2} R_{Lk}, k = 5, 6 \end{cases}. \tag{37}$$

According to the zero-setting matrix, the coil currents are solved. By substituting the coil currents into (16), the analytical formula of the compensation capacitor is obtained as

$$\begin{aligned} C_1 &= \frac{j \cdot \dot{I}_1}{\dot{I}_1 \cdot \omega^2 \cdot j \cdot L_1 + \omega \cdot \left(\dot{I}_3 \cdot X_{13} + \dot{I}_6 \cdot X_{16} + \dot{I}_5 \cdot X_{15}\right)} \\ C_2 &= \frac{j \cdot \dot{I}_2}{\dot{I}_2 \cdot \omega^2 \cdot j \cdot L_2 + \omega \cdot \dot{I}_4 \cdot X_{24}} \\ C_3 &= \frac{j \cdot \dot{I}_3}{\dot{I}_3 \cdot \omega^2 \cdot j \cdot L_3 + \omega \cdot \left(\dot{I}_1 \cdot X_{31} + \dot{I}_5 \cdot X_{35} + \dot{I}_6 \cdot X_{36}\right)} \\ C_4 &= \frac{j \cdot \dot{I}_4}{\dot{I}_4 \cdot \omega^2 \cdot j \cdot L_4 + \omega \cdot \dot{I}_2 \cdot X_{42}} \\ C_5 &= \frac{j \cdot \dot{I}_5}{\dot{I}_5 \cdot \omega^2 \cdot j \cdot L_5 + \omega \cdot \left(\dot{I}_1 \cdot X_{51} + \dot{I}_3 \cdot X_{53} + \dot{I}_6 \cdot X_{56}\right)} \\ C_6 &= \frac{j \cdot \dot{I}_6}{\dot{I}_6 \cdot \omega^2 \cdot j \cdot L_6 + \omega \cdot \left(\dot{I}_1 \cdot X_{61} + \dot{I}_3 \cdot X_{63} + \dot{I}_5 \cdot X_{65}\right)}. \end{aligned} \tag{38}$$

REFERENCES

[1] S. Y. R. Hui, W. Zhong, and C. K. Lee, “A critical review of recent progress in mid-range wireless power transfer,” *IEEE Trans. Power Electron.*, vol. 29, no. 9, pp. 4500–4511, Sep. 2014.

[2] S. Moon, B.-C. Kim, S.-Y. Cho, C.-H. Ahn, and G.-W. Moon, “Analysis and design of a wireless power transfer system with an intermediate coil for high efficiency,” *IEEE Trans. Ind. Electron.*, vol. 61, no. 11, pp. 5861–5870, Nov. 2014.

[3] K. Lee and S. H. Chae, “Power transfer efficiency analysis of intermediate-resonator for wireless power transfer,” *IEEE Trans. Power Electron.*, vol. 33, no. 3, pp. 2484–2493, Mar. 2018.

[4] Y. Li, Q. Xu, T. Lin, J. Hu, Z. He, and R. Mai, “Analysis and design of load-independent output current or output voltage of a three-coil wireless power transfer system,” *IEEE Trans. Transp. Electrific.*, vol. 4, no. 2, pp. 364–375, Jun. 2018.

[5] Y. Yang, H. W. Rebecca Liang, S. C. Tan, and S. Y. Ron Hui, “Design of a wireless power modulator for wireless power transfer systems,” in *Proc. IEEE 12th Energy Convers. Congr. Expo. - Asia*, 2021, pp. 816–820.

[6] M. Takasaki, Y. Miura, and T. Ise, “Wireless power transfer system for gate power supplies of modular multilevel converters,” in *Proc. IEEE 8th Int. Power Electron. Motion Control Conf.*, 2016, pp. 3183–3190.

[7] Z. Dongye, Y. Wang, H. Zhang, S. Zheng, X. Lu, and F. Lu, “A 4kV/100A SiC MOSFETs-based solid state dc circuit breaker with low stray inductances and powered by a load-independent wireless power transfer system,” in *Proc. IEEE Energy Convers. Congr. Expo.*, 2020, pp. 1279–1283.

[8] K. Kusaka, K. Orikawa, J. -i. Itoh, K. Morita, and K. Hirao, “Isolation system with wireless power transfer for multiple gate driver supplies of a medium voltage inverter,” in *Proc. Int. Power Electron. Conf.*, 2014, pp. 191–198.

[9] C. Zhang, D. Lin, N. Tang, and S. Y. R. Hui, “A novel electric insulation string structure with high-voltage insulation and wireless power transfer capabilities,” *IEEE Trans. Power Electron.*, vol. 33, no. 1, pp. 87–96, Jan. 2018.

[10] Y. Li, L. Gui, Y. Jiang, R. Jing, Y. Li, and Z. He, “Optimal configuration of single-layer domino-coils with uniform spacing for online monitoring equipment in smart grid,” *IEEE Trans. Power Electron.*, vol. 39, no. 11, pp. 14307–14317, Nov. 2024.

[11] P. Gu, Y. Wang, Z. Liu, J. Mai, T. Li, and D. Xu, “Analysis and design of long-range IPT system with multi-load CV characteristics based on cylindrical solenoid coupler,” *IEEE Trans. Ind. Appl.*, vol. 59, no. 2, pp. 2363–2373, Mar./Apr. 2023.

[12] M. Q. Nguyen, S. Dubey, S. Rao, and C. Chiao, “Wireless power transfer via air and building materials using multiple repeaters,” in. *Proc. Texas Symp. Wireless Microw. Circuits Syst.*, 2014, pp. 1–4.

[13] M. Liu, M. Fu, Y. Wang, and C. Ma, “Battery cell equalization via megahertz multiple-receiver wireless power transfer,” *IEEE Trans. Power Electron.*, vol. 33, no. 5, pp. 4135–4144, May 2018.

[14] Z. Dong, S. Liu, X. Li, Z. Xu, and L. Yang, “A novel long-distance wireless power transfer system with constant current output based on domino-resonator,” *IEEE J. Emerg. Sel. Topics Power Electron.*, vol. 9, no. 2, pp. 2343–2355, Apr. 2021.

[15] S. Liu, Y. Feng, H. Chen, J. Wu, and X. He, “Multi-coil constant voltage output analysis based on state deconstruction for wireless power transfer system,” in *Proc. IEEE Energy Convers. Congr. Expo.*, 2021, pp. 5704–5708.

[16] X. Hou, Y. Su, Z. Zuo, X. Dai, and Y. Fei, “A novel analysis method based on quadratic eigenvalue problem for multirelay magnetic coupling wireless power transfer,” *IEEE Trans. Power Electron.*, vol. 36, no. 9, pp. 9907–9917, Sep. 2021.

[17] P. Gu et al., “A 2.5m long-range IPT system based on domino cylindrical solenoid coupler compensated respectively in layers,” *IEEE Trans. Ind. Electron.*, vol. 70, no. 2, pp. 1409–1420, Feb. 2023.

[18] X. Hou, H. Hu, Y. Su, Z. Liu, Z. Deng, and R. Deng, “A multirelay wireless power transfer system with double-sided LCC compensation network for online monitoring equipment,” *IEEE J. Emerg. Sel. Topics Power Electron.*, vol. 11, no. 1, pp. 1262–1271, Feb. 2023.

[19] J. Wang et al., “Communication-free long-distance wireless charging system for battery load with adaptive switching of constant voltage and constant current,” *IEEE Trans. Transp. Electrific.*, vol. 10, no. 2, pp. 2653–2662, Jun. 2024.

[20] Z. Yan et al., “A monitoring equipment charging system for HVTL based on domino-resonator WPT with constant current or constant voltage output,” *IEEE Trans. Power Electron.*, vol. 37, no. 3, pp. 3668–3680, Mar. 2022.

[21] B. Wunsch, D. Zhelev, and B. Oedegard, “Externally-fed auxiliary power supply of MMC converter cells,” in *Proc. 18th Eur. Conf. Power Electron. Appl.*, 2016, pp. 1–10.

[22] B. L. Cannon, J. F. Hoburg, D. D. Stancil, and S. C. Goldstein, “Magnetic resonant coupling as a potential means for wireless power transfer to multiple small receivers,” *IEEE Trans. Power Electron.*, vol. 24, no. 7, pp. 1819–1825, Jul. 2009.

[23] D. Ahn and S. Hong, “Effect of coupling between multiple transmitters or multiple receivers on wireless power transfer,” *IEEE Trans. Ind. Electron.*, vol. 60, no. 7, pp. 2602–2613, Jul. 2013.

[24] Y. Zhang, T. Lu, Z. Zhao, F. He, K. Chen, and L. Yuan, “Employing load coils for multiple loads of resonant wireless power transfer,” *IEEE Trans. Power Electron.*, vol. 30, no. 11, pp. 6174–6181, Nov. 2015.

[25] C. Cheng, Z. Zhou, W. Li, C. Zhu, Z. Deng, and C. C. Mi, “A multi-load wireless power transfer system with series-parallel-series compensation,” *IEEE Trans. Power Electron.*, vol. 34, no. 8, pp. 7126–7130, Aug. 2019.

[26] C. Cheng et al., “A load-independent LCC-compensated wireless power transfer system for multiple loads with a compact coupler design,” *IEEE Trans. Ind. Electron.*, vol. 67, no. 6, pp. 4507–4515, Jun. 2020.

[27] Z. Dongye et al., “An S-CLC compensated load-independent inductive power relay system with constant voltage outputs,” *IEEE Trans. Power Electron.*, vol. 36, no. 5, pp. 5157–5168, May 2021.

[28] C. Cheng, Z. Zhou, W. Li, Z. Deng, and C. C. Mi, “A power relay system with multiple loads using asymmetrical coil design,” *IEEE Trans. Ind. Electron.*, vol. 68, no. 2, pp. 1188–1196, Feb. 2021.

[29] Z. Zhou, Z. Deng, C. Cheng, W. Li, F. Li, and C. Mi, “A wireless power transfer system with multiple constant current and constant voltage outputs,” in. *Proc. IEEE Energy Convers. Congr. Expo.*, 2019, pp. 4976–4981.

[30] Y. Wang, Z. Dongye, H. Zhang, C. Zhu, and F. Lu, “A domino-type load-independent inductive power transfer system with hybrid constant-current and constant-voltage outputs,” *IEEE Trans. Power Electron.*, vol. 36, no. 8, pp. 8824–8834, Aug. 2021.

[31] Z. Zhang et al., “A dynamic wireless power transfer system using dc controlled variable inductor for segment transmitter automatic switching,” *IEEE Trans. Power Electron.*, vol. 40, no. 1, pp. 23–27, Jan. 2025.

[32] C. Cheng, W. Li, Z. Zhou, Z. Deng, and C. Mi, “A load-independent wireless power transfer system with multiple constant voltage outputs,” *IEEE Trans. Power Electron.*, vol. 35, no. 4, pp. 3328–3331, Apr. 2020.

Yanling Li (Member, IEEE) received the B.Sc. and Ph.D. degrees in control theory and control engineering from Chongqing University, Chongqing, China, in 2008 and 2012, respectively.

She is currently an Associate Professor with the College of Electrical Engineering, Southwest Jiaotong University, Chengdu, China. Her research interests include wireless power transfer and its application in railway systems, power system stability, and control.

Yongkang Jiang received the B.Sc. degree in ship electronic and electrical engineering from Shanghai Maritime University, Shanghai, China, 2022. He is currentlyworking toward the M.Sc. degree in electrical engineering with Southwest Jiaotong University, Chengdu, China.

His main research interest focuses on wireless power transfer.

Weiqiang Liu is currently working toward the master’s degree in electrical engineering and automation with the School of Electrical Engineering, Southwest Jiaotong University, Chengdu, China.

His main research interest focuses on wireless power transfer.

Jingxian Zhao received the B.Sc. degree in automation from Southwest Petroleum University, Chengdu, China, in 2022. She is currently working toward the M.Sc. degree in electrical and information engineering with Southwest Jiaotong University, Chengdu, China.

Her current research interest focuses on the wireless power transfer.

Yong Li (Senior Member, IEEE) received the B.Sc. and Ph.D. degrees from the School of Electrical Engineering, Southwest Jiaotong University, Chengdu, China, in 2013 and 2017, respectively.

From 2017 to 2018, he was a Research Associate with the Department of Electrical Engineering, The Hong Kong Polytechnic University, Hong Kong, where he was a Post-Doctoral Fellow from 2018 to 2019. He is currently an Associate Professor with Southwest Jiaotong University. His main research interests include wireless power transfer and microgrids.

Zhengyou He (Senior Member, IEEE) received the B.Sc. and M.Sc. degrees in computational mechanics from Chongqing University, Chongqing, China, in 1992 and 1995, respectively, and the Ph.D. degree in electrical engineering from Southwest Jiaotong University, Chengdu, China, in 2001.

He is currently a Professor with the College of Electrical Engineering, Southwest Jiaotong University. His research interests include signal process and information theory applied to electrical power system, and application of wavelet transforms in power system.